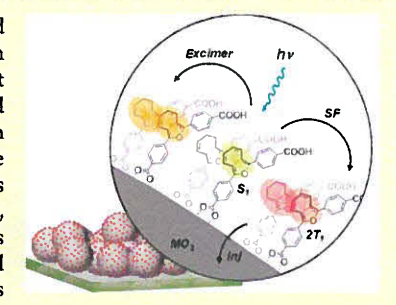
Diphenylisobenzofuran Bound to Nanocrystalline Metal Oxides: Excimer Formation, Singlet Fission, Electron Injection, and Low **Energy Sensitization**

Tanmay Banerjee,^{†,§} Sean P. Hill,^{†©} M. Alejandra Hermosilla-Palacios,[‡] Brandon D. Piercy,^{||} Jess Haney, Bryan Casale, A. Eugene DePrince, III, Mark D. Losego, Valeria D. Kleiman, and Kenneth Hanson*,†

Supporting Information

ABSTRACT: We report the photophysical properties of the dicarboxylated diphenylisobenzofuran dye (1) bound to nanocrystalline metal oxide surfaces. With increased surface loading of 1, emission from the films is significantly quenched but with a small amount of excimer emission at maximum surface loadings. Long-lived triplets were observed by ns TA spectroscopy that are consistent with singlet fission occurring on mesoporous ZrO₂. The evolution of these triplets, however, could not be convincingly resolved by our subnanosecond TA spectroscopy. Dye-sensitized devices composed of 1 on a TiO2lAl2O3 core-shell structure exhibited an unusual decrease, increase, and then decrease in Isc with respect to the thickness of Al₂O₃. In these films the Al₂O₃ acts as a tunneling barrier to slow electron injection from the singlet excited state such that singlet fission, and electron injection from the triplet state becomes competitive. Proof-of-principle self-assembled bilayer films that exhibit efficient triplet



energy transfer from a low energy absorbing dye to 1 is demonstrated as another step toward a SF-based DSSC that can circumvent the Shockley-Queisser limit.

■ INTRODUCTION

The maximum theoretical efficiency of a standard singlejunction solar cell is constrained to only 33% (a.k.a. the Shockley-Queisser (SQ) limit). Splitting a high energy photon into multiple lower energy excited states, also called multiple exciton generation (MEG), is an intriguing strategy to decrease losses due to thermalization and circumvent the SQ limit.2-4 MEG can occur at high efficiencies in inorganic nanoparticles, but they typically contain costly and hazardous transition metals like lead, cadmium, etc. and require high energy photons (<400 nm) that are limited under ambient solar flux. Singlet fission (SF) is an analogous MEG process that occurs in organic molecules and has been demonstrated in solution, ⁶ thin films, ⁷⁻¹¹ aggregates, ^{12,13} polymers, ⁷ covalent dyads, ¹⁴⁻¹⁷ and even biological systems. ¹⁸ In SF, a chromophore in a high energy singlet excited state allocates a portion of its excited state energy to a neighboring molecule in the ground state, and as a result, both molecules are converted into lower energy triplet excited states. 19

The primary motivation given for studying SF is to increase solar cell efficiencies; nevertheless, a majority of the SF research has been fundamental in nature, which provides insights into the energetic and structural requirements for high SF yields, ^{19,20} and the design of new molecules, ²¹⁻²⁴ but offers no clear path toward harnessing SF in a device. There are however several reports of using amorphous or polycrystalline thin films in organic photovoltaic or silicon sensitized architectures to harness SF. 25-29 External quantum efficiencies greater than 100% have been demonstrated in some of these systems, 27,30,31 but the overall device efficiencies are still relatively low.³² The low efficiency can be attributed to a lack of low energy light absorption, oxygen sensitivity of the chromophores, donor-acceptor dimerization at the interface, inefficient triplet charge separation, and/or charge carrier recombination. Many of these issues are in fact intrinsic difficulties with these particular molecules/architectures.33

Adhering SF molecules to a metal oxide surface, as in dyesensitized solar cells (DSSCs), offers a unique scaffolding to not only facilitate intermolecular interactions like those necessary for SF¹⁹ but also provide a means of extracting charge from the triplet excited state without any issues arising from charge/exciton diffusion and polaron quenching. Despite its potential, there are only three reports of using metal oxide substrates to facilitate and harness SF. In the first

Received: September 3, 2018 Revised: November 7, 2018 Published: November 20, 2018



[†]Department of Chemistry and Biochemistry, Florida State University, Tallahassee, Florida 32306, United States

[‡]Department of Chemistry, University of Florida, PO BOX 117200, Gainesville, Florida 32611-7200, United States

^{||}School of Materials Science and Engineering, Georgia Institute of Technology, Atlanta, Georgia 30332, United States

example, Schrauben et al.³⁵ studied a long chain carboxylated derivative of 1,3-diphenylisobenzofuran (**DPIBF**) and physisorbed **DPIBF** on a TiO₂–ZrO₂, core–shell nanocrystalline surface. The authors observed a decrease and then a small increase in photocurrent with respect to ZrO₂ shell thickness for both molecules and this was likely attributed to SF but not definitively established. In a follow-up study, Pace et al. bound carboxylated tetracene and pentacene dyes directly to the TiO₂ surface.³⁶ Using TA spectroscopy the authors demonstrated SF at the interface but electron injection from the triplet excited state into the TiO₂ was not observed due to a lack of driving force for triplet dissociation at the interface. Recently, Kunzmann et al. reported 130% electron injection efficiency from the triplet excited states formed after SF in a carboxylated pentacene dimer into indium-doped ZnO.³⁷

Here we report the synthesis and coordination of 4,4'-(isobenzofuran-1,3-diyl)dibenzoic acid (1) (Figure 1) directly

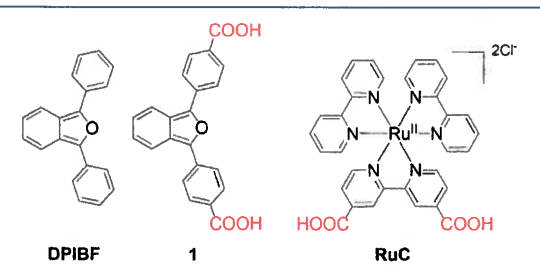


Figure 1. Structures of 1,3-diphenylisobenzofuran (DPIBF), 4,4'-(isobenzofuran-1,3-diyl)dibenzoic acid (1), and $Ru(bpy)_2(4,4'-(COOH)_2bpy)Cl_2$ (RuC).

to a metal oxide surface and study its photophysical properties including multimolecular processes like excimer formation and singlet fission. Molecule 1 can be synthesized in appreciable yields and is relatively stable against decomposition due to photo-oxidation during synthesis or photophysical studies. Steady-state and time-resolved emission/absorption are used to monitor the excited state dynamics including the formation of triplet excited states which is consistent with SF occurring at the interface. Device measurements indicate that these triplet excited states can be harvested in a dye sensitized solar cell. Furthermore, we demonstrate bilayer self-assembly as an effective means of incorporating a low energy absorber into this SF-based DSSC scheme as an additional stepping stone toward surpassing the SQ limit.

EXPERIMENTAL SECTION

Materials. Zinc acetate dihydrate, 4-bromobenzoic acid, oxalyl chloride, 2-amino-2-methyl-1-propanol, and thionyl chloride were obtained from Sigma-Aldrich and used as received. 3-Methoxyphthalide has been obtained from Alfa Aesar. All other reagents and solvents (analytical reagent grade) have been purchased from Alfa Aesar and used without further purification. Solvents used in synthesis have been dried and degassed prior to use.

Fluorine-doped tin oxide (FTO) coated glass (sheet resistance 15 Ω \Box ⁻¹) was purchased from Hartford Glass Co. Meltonix film (1170–25) and Vac'n Fill Syringe (65209) were purchased from Solaronix. Micro glass cover slides (18 \times 18 mm) were obtained from VWR. ZrO_2 and TiO_2 pastes were prepared following a previously reported procedure. ³⁸

Synthesis. RuC,³⁹ DPPA,⁴⁰ and Co(bpy)₃²⁺⁴¹ and Co-(bpy)₃³⁺⁴¹ were obtained from previous studies. Synthesis and complete characterization of 1 is described in the Supporting Information.

Dye Loading. Dye loading onto the mesoporous metal oxide films was performed as described in the manuscript. Surface coverages (Γ in mol cm⁻²) for 1 are described with the expression $\Gamma = \{A(\lambda)/\varepsilon(\lambda)\}/1000$, where ε is the molar extinction coefficient in DMSO and $A(\lambda)$ is the maximum absorbance of the slides. Adsorption isotherms were fit using Γ = Γ_{max} (($K_{\text{ad}} \times [1]$)/(1 + $K_{\text{ad}} \times [1]$)) to give the equilibrium adsorption constant (K_{ad}) and maximum surface coverage (Γ_{max}) in accord with the Langmuir isotherm model. For the 1 and RuC coloaded ZrO2 samples for transient absorption (TA) experiments, 1 was loaded onto a ZrO2 film from a 200 μM DMSO solution for 30 min, and then soaked in a 200 μM RuC solution in methanol for 1 min. For 1 and DPPA monolayer TiO₂ samples, films were soaked into their respective 200 μ M loading solutions in DMSO for 2 h and overnight, respectively. All films were thoroughly rinsed with MeCN to remove any physisorbed molecules and dried in a stream of nitrogen gas.

Theoretical Calculations. Optimal geometries and theoretical estimates of $E(T_1)$ and $E(S_1)$ for DPIBF and 1 were obtained from density functional theory (DFT). All computations were performed using the B3LYP functional and the 6-311++G(2d,p) basis set, as implemented in Q-Chem 4.4. For DPIBF, two optimal structures were located that differ in the relative orientation of the phenyl rings; these structures correspond to the C_s and C₂ isomers discussed in ref 42. At the B3LYP/6-311++G(2d,p) level of theory, these isomers differ in energy by roughly 0.1 kcal mol-1. Similarly, two isomers of 1 were identified that differ in energy by less than 0.1 kcal mol⁻¹. Estimates of $E(T_1)$ and $E(S_1)$ for each isomer of DPIBF and 1 were computed using time-dependent DFT. As with the ground-state energies, excitation energies obtained at the C_s and C₂ geometries were essentially identical; estimates of $E(T_1)$ and $E(S_1)$ reported below correspond to

the C, isomers. Cell Assembly. Samples for photophysical and photovoltaic measurements were prepared following our previously published procedure. 40,41 Briefly, FTO glass was cut into 2.2 × 2.2 cm (for ZrO_2) or 2 × 2.5 cm (for TiO_2) squares pieces and an active area of 1 cm² metal oxide was prepared by doctor blading TiO2 or ZrO2 sol gel paste (1 layer Scotch tape) and sintering following previously published procedures. 40,41 Dye loading was performed as described in the manuscript. A small hole (d = 1.1 mm) was drilled into the corner of the 2.2×2.2 cm (or 2×2.5 cm for TiO₂ cells) glass slide that does not have metal oxide. For the electrochemical cells, with TiO2, the counter electrode was prepared by dropcasting 50 μ L of a 5 mM H2PtCl6 solution in ethanol that was heat dried at 400 °C for 15 min. A 3 mm wide 2.2 × 2.2 cm Meltonix film was placed between the two glass slides and the entire ensemble was heated to ~150 °C for 7 s. For the TiO2 samples, the two glass slides were offset by ~5 mm to ensure sufficient area for electrode contacts. The cells were then transferred to a glovebox where dry and oxygen free solvent (MeCN for the ZrO₂ samples, and a solution of 0.1 M LiClO₄ and 0.2 M/0.02 M Co(bpy)₃^{2+/3+} in MeCN for the TiO₂ samples) was injected using a Vac'n Fill Syringe (Solaronix) through the 1 mm hole to fill the interior of the cells. The cell was then sealed with a

Meltonix film and a small piece of micro glass cover slide that covers the hole used for solvent injection.

Atomic Layer Deposition. A viscous-flow ALD reactor was used to deposit Al₂O₃ at 150 °C and 1.5 Torr. Ultrapure nitrogen (99.999%, Airgas) was used as a carrier gas. Process gas lines were maintained at 110 °C and precursors were kept at room temperature. Al₂O₃ layers were deposited using sequential doses of trimethylaluminum (TMA, Strem), and H_2O , using a dose sequence of 0.2 s/45 s/0.1 s/30 s (TMA/ N_2 purge/ H_2O/N_2 purge). Prior to deposition, the photoanodes were held in the reactor at 150 °C for 15 min in flowing dry nitrogen to remove adsorbed moisture.

Analytical Methods. 1H NMR spectra were recorded on a Bruker 600 MHz FT NMR (Model: Avance-DPX 600) and the spectral shifts were calibrated with respect to residual solvent peaks. ESI-MS measurements were carried out on a JEOL AccuTOF JMS-T100LC instrument.

Photophysical and Electrochemical Measurements. Attenuated Total Reflectance Infrared (ATR-IR). These absorption spectra were recorded using a Bruker Alpha FTIR spectrometer (SiC Glowbar source, DTGS detector) with a Platinum ATR quickSnap sampling module (single reflection diamond crystal). Spectra were obtained by placing dry, derivatized ZrO2 slides active side down (or the compound itself in a powder form for molecule characterization) on the diamond face and data was acquired from 800 to 1800 cm⁻¹ at a resolution of 4 cm⁻¹. All ATR-IR spectra are reported in absorbance with a blank versus atmosphere.

UV-Vis Absorption Spectra. These were recorded on an Agilent 8453 photodiode array spectrophotometer. Extinction coefficients for 1 in DMSO were determined from the absorption spectra of solutions having a known concentration of chromophore in a 1 cm × 1 cm quartz cuvette. Thin film absorption spectra were obtained by placing dry, derivatized TiO₂ and ZrO₂ slides perpendicular to the detection beam path.

Cyclic Voltammetry (CV). These measurements were performed by using a CH Instruments Model CHI630E Series Electrochemical Workstation with a solution of 1 in 0.1 M TBAClO₄ MeCN using a glassy carbon working electrode, a platinum wire auxiliary electrode and a Ag wire reference electrode. Ferrocene (0.63 V vs. NHE) was added as an internal standard. All potentials are converted and quoted with respect to the normal hydrogen electrode (NHE).

Steady-State Emission. These data were collected at room temperature using an Edinburgh FLS980 fluorescence spectrometer. The samples were excited using the output from a housed 450 W Xe lamp/single grating (1800 lines/mm, 250 nm blaze) Czerny-Turner monochromator. Emission from the sample was first passed through an appropriate long-pass filter and then a single grating (1800 lines/mm, 500 nm blaze) Czerny-Turner monochromator and finally detected by a Peltier-cooled Hamamatsu R928 photomultiplier tube.

Absolute Emission Quantum Yields. For 1c and 1, and for ZrO2-1 in MeCN samples, these values were acquired using an integrating sphere incorporated into the Edinburgh FLS980 fluorescence spectrometer. For 1c and 1, the compounds were dissolved in DMSO (O.D.~ 0.1 at λ_{exc}) in a standard 1 cm \times 1 cm quartz fluorescence cuvette. ZrO2-1 in MeCN samples were prepared and sealed in the sandwich cell-type architecture as described above and placed in the center of the sphere which includes a movable mirror for direct or indirect excitation (De Mello Method).44 Emission quantum yields

were then acquired and calculated following literature procedure.45

Time-Resolved Emission. For ZrO2-1 in MeCN, it was acquired using the FLS980's time-correlated single-photon counting capability (1024 channels; 100 ns window) with data collection for 5000 counts. Excitation was provided by an Edinburgh EPL-405 diode laser (405 ± 5 nm, 60 ps fwhm). Kinetics were fit to the least number of exponentials using the 3.4.2 version of FAST software of Edinburgh Instruments Ltd. following eq 1. A reconvolution fit was done for exponential component analysis.

$$y = \sum_{i} A_i e^{-ki \cdot x} + y_0 \tag{1}$$

Nanosecond Transient Absorption (TA). These measurements were carried out by inserting sealed samples $(2 \times 2 \text{ cm})$ with a 1×1 cm active area) perpendicular to the light source in a collinear arrangement. The spectrometer is composed of a Continuum Surelite EX Nd:YAG laser combined with a Continuum Horizon OPO (532 nm, 5-7 ns, operated at 1 Hz, beam diameter ~0.5 cm, 2.5-5 mJ/pulse) integrated into a commercially available Edinburgh LP980 laser flash photolysis spectrometer system. White light probe pulses generated by a pulsed 150 W Xe lamp were passed through the sample, focused into the spectrometer, then detected by intensified Andor iStar CCD camera. Time-resolved emission scans were passed through a TMS302-A monochromator (1800 grooves/ mm grating) with a 300 mm focal length in Czerny Turner configuration and detected by a Hamamatsu R928 side window PMT. Detector outputs were processed using Edinburgh's L900 (version 8.2.3, build 0) software package. As with emission, kinetics were fit to an exponential function.

Ultrafast Transient Absorption (TA) Measurements. These were performed on a laser system configured for pump-probe measurements. A train of 100 fs pulses with 1 kHz repetition rate was produced by a mode-locked Ti:sapphire oscillator (Coherent Vitara-S pumped by 5 W Coherent Verdi 532 nm output) in conjunction with a regenerative amplifier (Coherent Astrella). The parent beam (6.2 W) was split along two separate pathways; approximately 4.5 W were directed to Coherent OPerA Solo to generate the visible pump, while the other beam (1.5 W) was sent to an Ultrafastsystem Helios instrument to generate the visible broadband continuum through a sapphire window. The Ultrafastsystem Helios pump-probe setup is obtained with a 8 ns delay stage and a small angle noncollinear alignment. The direction of polarization of the pump beam was fixed at the magic angle with respect to that of the probe beam. The films were rastered during the experiments and the chosen wavelength for excitation was 405 nm with 50 nJ per pulse at sample position. The solutions were prepared in a glovebox and stirred during the experiments, and the chosen wavelength for excitation was 420 nm with 50 nJ per pulse at sample position.

Current Density-Voltage (I-V). These curves were measured using a Keithley Model 2400 Source Meter while irradiating the devices with an AM1.5 solar spectrum generated from a 300 W xenon arc lamp (Ushio, UXL-302-O) enclosed in an Oriel Research Arc-lamp Housing (Newport, 67005) with the light output passed through an AM 1.5 Global filter (Newport, 81094). The light intensity was measured using a calibrated reference cell and meter (Newport, 91150 V). Additional details can be found in our previous report.4

Scheme 1. Synthesis of 1^a

^aKey: $i = (COCl)_2$, cat. DMF in toluene; ii = 2-amino-2-methyl-1-propanol in DCM; $iii = SOCl_2$, iv = Mg, catalytic I_2 in THF, v = THF at 0 °C, vi = aqueous HCl.

RESULTS AND DISCUSSION

Synthesis. Compound 1 was synthesized following a literature procedure, 47 albeit with considerable modifications (Scheme 1). Briefly, 4-bromobenzoic acid was converted to the corresponding acyl chloride and then reacted with the aminopropanol compound to give 1a. Oxalyl chloride was used as the acylating agent and the reaction was complete in 4 h as compared to 24 h reaction time with thionyl chloride. The benzamide was cyclized to the corresponding oxazoline (1b) and then used to form the organomagnesium bromide reagent for a Grignard reaction with 3-methoxyphthalide to give the diphenylisobenzofuran precursor 1c. The time to complete Grignard reagent formation was significantly reduced by heating the Mg turnings in I2 vapor before addition of 1b. It is worth noting that 1c is a white powder with remarkably low extinction coefficient of 7.3 M⁻¹ cm⁻¹ (at 437 nm) in DMSO and is less emissive ($\Phi = 0.29$) than the product 1 ($\Phi = 0.88$). In terms of isolating 1c, the lack of color and only weakly emission were unexpected and initially gave us difficulties in identifying the product in that we were anticipating photophysics similar to 1. The origin of such remarkable difference in the photophysical properties is not clear to us at this time. An in-depth theoretical analysis (e.g., transition dipole, symmetry, orbital overlap, etc.) of 1 and 1c will likely be necessary to elucidate the origin of this unusual behavior.

Finally, the desired product (1) was obtained by a hydrolysis of the oxazoline groups in 1c to carboxylic acids. The red precipitate formed was washed repeatedly with cold water until the aqueous eluent was at a neutral pH, and then the solid was dried to give the spectroscopically pure product (1). Redissolving and refluxing the product in aqueous NaOH followed by reprecipitation, as reported previously, did not increase the purity of the compound but significantly decreased the reaction yield.

Compound 1 was selected as our target molecule because it is a derivative of 1,3-diphenylisobenzofuran (DPIBF), a well-known SF dye that has been extensively studied in crystals/thin films/solutions, and shown to have a maximum SF yield of nearly 200%. 11,14,48-52 Also, it can readily be synthesized with surface binding groups and has sufficient excited state potential

for electron transfer from its triplet excited state into TiO₂ (vide infra).

Photophysics in Solution. The absorption spectrum of 1 in DMSO is characterized by a vibronically resolved low energy band with an extinction coefficient of 37,300 M⁻¹ cm⁻¹ at 440 nm (Figure 2). Additional high energy absorption bands

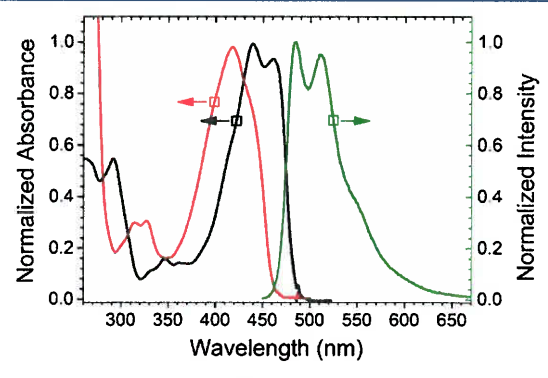


Figure 2. Normalized absorption (black) and emission spectrum (green) of 1 in DMSO at room temperature. For comparison, the absorption spectrum of DPIBF in DMSO is shown in red.

can be seen at 345 and 290 nm. The absorption features for 1 are similar but bathochromically shifted by \sim 0.2 eV relative to the parent **DPIBF** due to the electron withdrawing nature of the -COOH groups. In DMSO at room temperature, the compound exhibits vibronically structured blue-green emission ($\lambda_{max} = 485$ and 510 nm) with a quantum yield of 88% and a lifetime of 4.0 ns. Attempts to observe phosphorescent emission from 1 even at low temperature (77 K) and in the presence of MeI were unsuccessful.

Given that the energies of the singlet and triplet excited states are crucial to realizing SF, DFT calculations were performed on both **DPIBF** and 1 in the gas phase using the B3LYP functional and 6-311++G(2d,p) basis set (see Experimental Section for details). The singlet $(E(S_1))$ and triplet $(E(T_1))$ excited state energies for 1 were found to be 2.65 and 1.41 eV, respectively. Because $E(S_1)$ is less than $2 \times E(T_1)$, these computations suggest that SF is an endothermic

process by ~0.17 eV. Under the same conditions, the calculated energies for **DPIBF** $(E(S_1) = 2.84 \text{ eV})$ and $E(T_1) = 1.53 \text{ eV})$ also suggest a ~0.22 eV endothermic process. The estimate for **DPIBF** $E(S_1)$ and $E(T_1)$ are slightly higher than the experimentally determined values of 2.73 and 1.41 eV, respectively. ⁴⁸ Given that **DPIBF** is known to undergo SF in near unity quantum yields ($\Phi_{SF} \approx 200\%$), the similarity in the predicted relative values of $E(T_1)$ and $E(S_1)$ in **DPIBF** and 1, as well as the prediction that SF is slightly less endothermic for 1, suggest that SF from 1 is feasible.

Electrochemical Properties. Compound 1 in MeCN exhibits an irreversible oxidative wave with an oxidation potential $(E_{1/2}^{\text{ox}})$ of 1.03 V vs NHE as determined using differential pulse voltammetry. A singlet excited state reduction potential $(E_{1/2(S1)})$ of -1.59 V vs NHE was calculated using the equation $E_{1/2(S1)} = E_{1/2}^{\text{ox}} - \Delta G_{S_{1}}$, where the singlet excited state energy ($\Delta G_{S_1} = 2.62$ eV) was determined from the intersection of the normalized absorption and emission spectra of 1.40 The triplet excited state reduction potential $(E_{1/2(T_1)})$ was calculated to be -0.4 V using the theoretically calculated triplet excited state energy ($\Delta G_{T_1} = 1.41 \text{ eV}$), and the equation $E_{1/2(T_1)} = E_{1/2}^{\text{ox}} - \Delta G_{T_1}$. From these values, 1 has excited state potentials comparable to the conduction band of TiO_2 (E_{TiO_2} CB $\approx -0.5 \text{ V vs NHE})^{53}$ indicating that it is not unreasonable to expect electron transfer from the S₁ or T₁ state of 1 into TiO₂, albeit much slower and less efficiently from the latter, T₁ state.

Surface Loading. Surface functionalization was achieved by soaking nanocrystalline ZrO2 films in DMSO solutions of 1 with loading monitored using UV-vis spectroscopy (Figure 3a). The absorption energies of 1 on ZrO2 (herein referred to as ZrO2-1) are similar to that in solution but with a slight broadening that is common for surface adsorbed dyes.⁵⁴ Surface loading of 1 obeys Langmuir isotherm behavior (Figure 3a, inset) with a maximum surface coverage of 9.0 × 10⁻⁸ mol·cm⁻² that can be achieved by soaking ZrO₂ films in a 200 μM solution of 1 for a period of 2 h. Following our previously published procedure, 54 the center-to-center distance between 1 molecules (d₁₋₁) can be calculated using the ZrO₂ surface area of 115 m²/g, a maximum absorbance of 1.8 for a \sim 3 μ m thick film, and an extinction of 37 300 M⁻¹ cm⁻¹ at the peak maxima. From the surface area, the total number of dye molecules, and assuming hexagonal packing of spherical molecules on the surface, we estimate a d_{1-1} of 9.5 Å. This spacing is similar to that observed for 4,4-(anthracene-9,10diyl)bis(4,1-phenylene) diphosphonic acid (DPPA) (d = 8.6A), our control dye for photocurrent measurements (vide infra), and is indicative of complete, close packing monolayer coverage of the metal oxide surface. 55 This average intermolecular distance (9.5 Å) is comparable to those observed in DPIBF crystals which can range from 7 to 11 Å depending on which molecular packing pairs are selected.49

Two important observations can be noted from Figure 3a. First, there is no evidence for ground state dye aggregation even at the maximum surface loadings and second, the surface coverage (i.e., average intermolecular distance) can readily be controlled by varying the concentration of the loading solution.

Steady-State and Time-Resolved Emission. Spectroscopic sandwich cells of the ZrO₂-1 films in MeCN were prepared in a nitrogen glovebox to ensure exclusion of oxygen and mitigate concerns with atmosphere-induced decomposition of the samples. Nanocrystalline ZrO₂ was selected as the

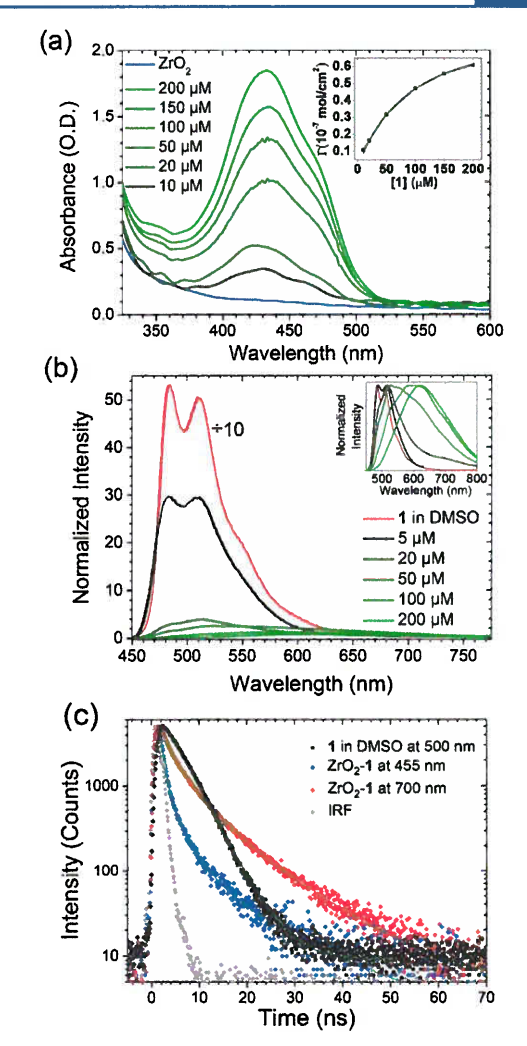


Figure 3. (a) UV—vis absorption spectra of ZrO_2 -1 with respect to the concentration of the loading solution (inset: Langmuir isotherm), (b) relative and normalized (inset) emission for ZrO_2 -1 in MeCN with respect to loading concentration ($\lambda_{ex} = 420$ nm), and (c) time-resolved emission decay traces for 1 in DMSO and fully loaded ZrO_2 -1 in MeCN ($\lambda_{ex} = 405$ nm).

substrate for emission studies because its relatively high conduction band energy $(E_{ZrO_2}^{CB} = -1.8 \text{ V vs NHE})^{56}$ prevents excited state quenching via electron transfer to the substrate. For example, DPPA $(E_{1/2}(S_1)) = -1.65 \text{ V vs NHE})$, which has a greater driving force for excited state electron transfer than 1 $(E_{1/2}(S_1))$ of -1.59 V vs NHE), exhibits similar quantum yield and lifetime in solution and bound to ZrO_2 . ^{40,54,57,58} Because of the >50 mV lower driving force for 1 than DPPA and the >200 mV thermodynamically unfavorable energetics, we anticipate that electron transfer from 1 to ZrO_2 , if any, is negligible.

The emission spectrum and quantum yield for ZrO₂-1 with respect to surface loading concentration can be seen in Figure 3b and Table S1. The emission quantum yield for the film with the lowest surface loading (5 μ M; 0.56 \times 10⁻⁸ mol·cm⁻²) is 0.05 which is ~95% quenched relative to 1 in solution (Φ = 0.88). With increasing surface loading there is a continuous

Table 1. Photoluminescent Properties of 1 in DMSO and Fully Loaded ZrO_2 -1 in MeCN (λ_{ex} = 405 nm)

		τ (ns)				
sample	λ _{em} (nm)					Φ_{PL}
1 in DMSO	500	4.0				0.88
ZrO ₂ -1	455	<1 (75%)	3.3 (16%)	8.0 (4%)	17.3 (5%)	0.01
	700	<1 (23%)	4.2 (44%)	11.0 (32%)	22.6 (1%)	

decrease in emission intensity with the fully loaded film being ~99% quenched relative to solution. This observation is consistent with increased loading decreasing the average intermolecular distance and increasing the likelihood of bimolecular events like SF. However, it is worth noting that in addition to decreased emission quantum yield there is a spectral shift from 480 to 620 nm and peak broadening with increased surface loading. Similar behavior has been observed in crystalline solids of DPIBF and is attributed to emission from an excimer state. 49,5

Time-resolved emission decays for 1 in DMSO and the fully loaded ZrO2-1 in MeCN can be seen in Figure 3c. While the emission decay for 1 in solution can be fit with a single exponential function ($\tau = 4.0$ ns), the emission kinetics for the films were complex. The complexity can be attributed to both the inhomogeneity of the local environment of the molecules and the introduction of new excited state processes. 59,61

The decay kinetics at 455 and 700 nm (without and with excimer emission, respectively) contain at least 4 components as summarized in Table 1. At 455 nm, the fastest component (<1 ns) which dominates the decay, is on time scales approaching the IRF and may correspond to the dynamics of SF or excimer formation. The 3-5 ns component is comparable to the decay kinetics in solution and can presumably be attributed to emission from the singlet excited state of 1 in the absence of additional quenching events. Interestingly, a notable fraction (9%) of the decay at 455 nm has a longer lifetime (>8 ns) than 1 in solution. Similar longlived emission from the singlet manifold has been observed in crystalline DPIBF and is often attributed to delayed fluorescence from triplet-triplet annihilation following SF. Triplet-triplet annihilation is known to occur at dye-semiconductor interfaces. 39,40,61,62

At 700 nm, there is also a notable (32%) long-lived emission (>11 ns) from the excimer state. Surprisingly, the emission lifetime for the excimer is longer than that from the monomer. Similar long-lived excimer emission has been observed in other systems, but the origin of the elongated lifetime remains unclear. ⁶⁰ If we assume similar nonradiative decay channels (C-C and C-O bond and solvent vibrations) and presumably equal if not greater nonradiative decay rates (k_{nr}) , the increased lifetime suggests a lower radiative rate (k_r) for the excimer versus the monomer. Quantum yield measurements for the excimer emission as well as temperature dependent measurements will likely be needed to elucidate the origin of this slowed decay from the excimer state.

It is well-known that an external magnetic field influences the amount of singlet character in correlated triplet pairs which can, but does not always, manifest as changes in the prompt and delayed fluorescence rates/yields in SF materials. 20,63,64 For ZrO2-1 in MeCN we did not observe any noticeable change in the emission intensity or the decay kinetics with respect to an externally applied magnetic field up to 0.55 T (Figure S1). The effect of magnetic field on emission is determined by the zero-field splitting parameters D and E for a

particular molecule, and by the energy difference between the ¹(TT), ³(TT), and ⁵(TT) states which is dependent on the interaction between the neighboring molecules. 19,20 Interestingly, while magnetic field dependence of SF for molecules like tetracene and pentacene is known, 19,65-67 field dependence of SF for DPIBF molecules has not been reported and the zerofield splitting parameters for DPIBF are not known.52 possible that the maximum field applied here (0.5 T) is insufficient to observe a notable effect. Regardless, it is important to note that, as stated previously, the lack of magnetic field dependence does not preclude SF, but it instead can simply mean that the field dependence of SF for DPIBF is much weaker than for tetracene, for example. 19,6

Nanosecond Transient Absorption. Nanosecond to millisecond transient absorption spectroscopy was used to probe any long-lived, nonemissive states and the results can be seen in Figure 4. Following a 405 nm excitation of the fully

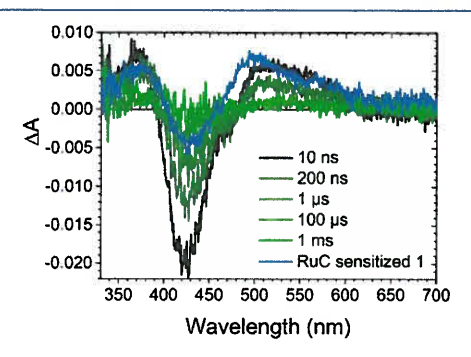


Figure 4. Room temperature TA spectra of ZrO_2 -1 in MeCN (λ_{exc} = 405 nm). The blue spectrum is for a ZrO2 film coloaded with 1 and RuC in MeCN, 10 µs after 520 nm excitation.

loaded ZrO₂-1 in MeCN sample, there is a bleach from 380 to 480 nm which coincides with loss of the ground state absorption, as well as new absorption features below 380 nm and from 480 to 650 nm. The decay kinetics were similar at all wavelengths with a lifetime of >250 μ s (Figure S2) suggesting that the spectra is dominated by a single species. Under the same measurement conditions, no absorption features were observed from 1 in DMSO due to its excited state decay within the instrument response (\sim 10 ns).

The long-lived TA spectral features for fully loaded ZrO2-1 closely resemble that of the triplet excited state of 1 generated via sensitization (blue spectrum in Figure 4). For sensitization measurements, ZrO2 films were coloaded with 1 and Ru(bpy)₂(4,4'-(COOH)₂bpy) (RuC). RuC was selected as the sensitizer because it readily binds to ZrO2, its triplet excited state energy $(E(T_1) = 2.01 \text{ eV})^{68}$ is greater than $1 (E(T_1) =$ 1.41 eV), and emission quenching studies in solution indicate near unity RuC-to-1 triplet energy transfer yields (Figure S4). The ZrO2-1/RuC film was pumped at 520 nm to selectively excite RuC. The spectrum 10 μ s after the laser pulse, well

beyond the excited state lifetime of the 3MLCT state of RuC (0.96 μ s), 69 shows the spectral features of the triplet excited state of 1. For the fully loaded ZrO_2 -1 films, the long-lived nature of the excited species as well as the similarity to the sensitized spectrum indicates that the triplet excited state of 1 is being generated at the nonsensitized interface. Since the intersystem crossing yield (Φ_{ISC}) is very low for organic molecules like DPIBF, 70 the appearance of the triplet absorption feature is consistent with SF occurring in ZrO_2 -1.

Femtosecond and Picosecond Transient Absorption. The transient absorption spectral changes prior to 1 ns for 1 solvated in THF were acquired and the results can be seen in Figure 5a. The ground state bleach and stimulated emission

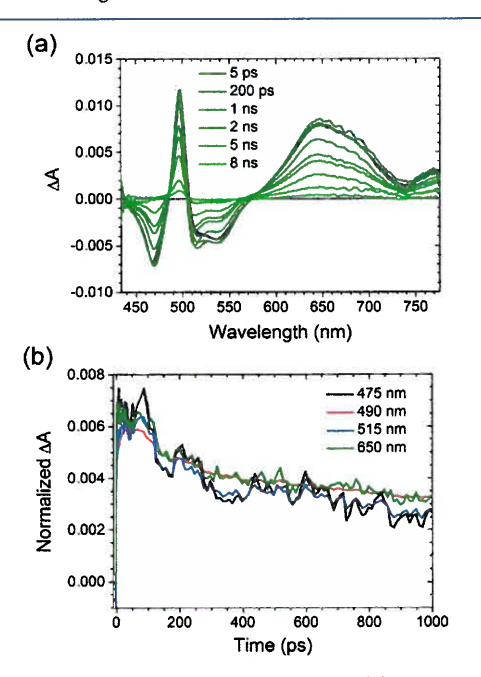


Figure 5. (a) Room temperature TA spectra and (b) kinetic traces at selected wavelengths for 1 in THF ($\lambda_{\rm exc} = 405$ nm).

from the singlet excited state can be seen at <480 and 510–570 nm, respectively. Additional positive absorption changes are observed at 500 nm and from 580 to 740 nm. These spectral features are similar to those of **DPIBF** singlet excited state in solution as reported previously.⁴⁸ In line with these observations, there were no absorption features indicative of a long-lived triplet excited state for 1 in solution.

Kinetic traces collected at the peak wavelengths of each of the aforementioned TA features have similar dynamics (Figure 5b) further supporting the point that, in solution, only one species, the single excited state (S_1) of 1, is present. The decay trace at 650 nm could be fit with a biexponential function giving lifetimes of 166.5 \pm 14.4 (35%) and 3.17 \pm 0.12 ns (65%). The longer component is comparable to the time-resolved emission decay kinetics (τ = 4.0 ns) and is consistent with relaxation from the singlet excited state of 1. The faster decay component has been observed for other diphenylisobenzofuran derivatives and could be attributed to solvent mediated structural relaxation of the excited state. ⁵¹

In contrast to 1 in solution, the subnanosecond TA spectral evolution of fully loaded ZrO₂-1 in MeCN is highly complex

(Figure 6a,b). At early times, there is a ground state bleach at λ < 490 nm accompanied by the appearance of broad positive

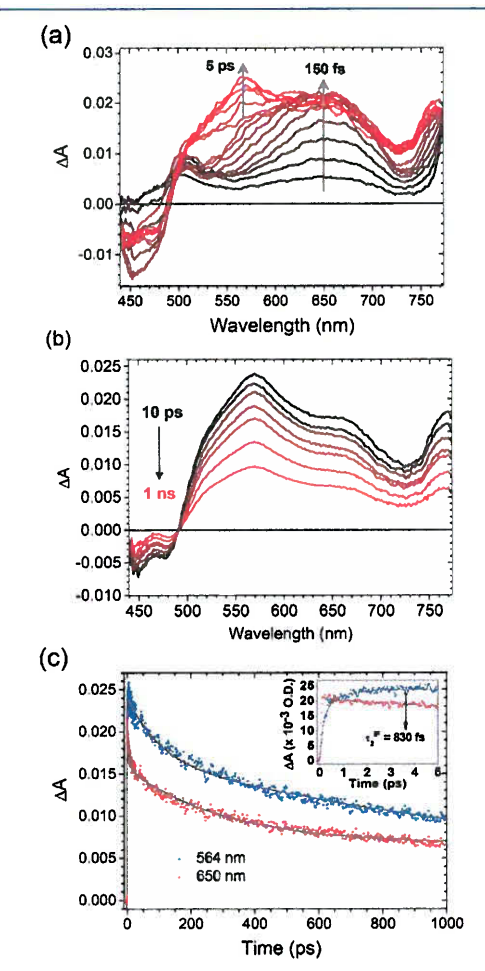


Figure 6. (a and b) Room temperature TA spectrum of fully loaded ZrO₂-1 in MeCN ($\lambda_{\rm exc}$ = 405 nm), and (c) single wavelength kinetic traces at 564 and 650 nm (inset: early time kinetics). For parts a and b, the color scheme depicts the transition in spectra from early (black) to later (red) time delays (0–5 ps in part a and 10 ps to 1 ns in part b).

absorption bands centered at 650 and 760 nm, and a sharp band at 510 nm. These features are consistent with the $S_1 \rightarrow S_n$ transition observed for 1 in solution. The amplitude of the S1 \rightarrow S_n absorption features increases during the first 150 fs followed by the appearance of a new absorption band in the 500-600 nm region that increases until 5 ps with a time constant $\sim 0.83 \pm 0.03$ ps (Figure 6c). The energy of this new feature is in agreement with the triplet ESA from ns TA and is consistent with SF time constants of 2 and 25 ps in polycrystalline thin solid films of 1,3-diphenylisobenzofuran.¹¹ Interestingly, from 150 fs to 5 ps, there is only a slight decrease in the ESA feature at 650 nm. It is possible that absorption from the excimer (as observed with emission spectroscopy) increases in this region as the $S_1 \rightarrow S_n$ ESA features are decreasing, and thus, there is no change in ΔA .⁵¹ Interestingly, both the 500-600 nm and the 650 nm absorption features decrease at similar rates, and the decay could be fitted with a tri- and biexponential function with time constants 6 ps (21.2%), 114 ps (53.5%), and >1 ns (25.3%) at 650 nm and 100 ps (30.4%) and >1 ns (69.6%) at 564 nm, respectively.

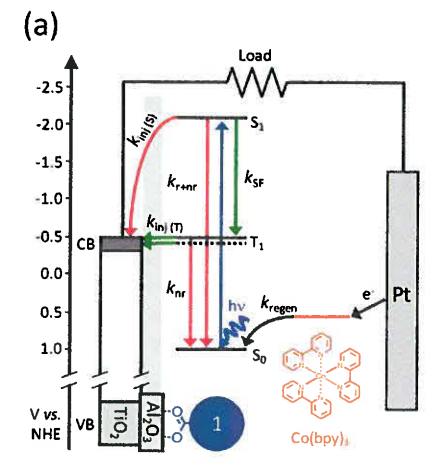
The similarity in decay kinetics for both features could be due to the equilibrium, excimer $\Rightarrow S_1 \Rightarrow (TT)$, as proposed by Schmidt et al., with the decay dictated by the fast step. Excimer-like low energy states in 1,3-diphenylisobenzofuran films have been observed and are said to reduce SF yields.4 Given a maximum possible triplet yield of 200% from SF, a triplet yield of ~60% was crudely estimated by comparing the bleach intensities at 5 ps vs 150 fs, if the 500-600 nm feature is indeed due to triplet absorption. However, given the relatively fast rate of decay, it is less likely that the 500-600 nm absorption features coincide with long-lived triplet states (>250 μ s) observed by ns TA. As the triplet species could not be clearly defined and the assignments remain ambiguous, we could not calculate a triplet yield using previously reported methods. 11,50

For some systems, charge transfer states have been proposed as intermediates in the SF process. 72,73 Thus, an alternative explanation is that we could be observing the formation of a charge-transfer (CT) state with cation features at 570 nm and the anion features at 650 nm. 48 This CT species may then evolve into the triplet correlated pair on longer time scales such that only the $T_1 \rightarrow T_n$ absorption feature is observed after 10 ns.

While we may be able to deconvolute the spectra by singular value decomposition analysis, without an appropriate model the results can be misleading. 50,51,71 Further subnanosecond TA studies with varied excitation wavelength, excitation fluence, temperature and solvent are needed to fully elucidate the triplet formation mechanism in ZrO₂-1. It is also important to note that the dynamics observed under the high fluence needed for spectroscopic measurements does not necessarily represent the behavior of ZrO₂-1, or any other SF material, under the relatively low photon flux of AM1.5 solar irradiation.

Device Measurements. Dye-sensitized solar cells were prepared in a standard sandwich cell architecture with dvefunctionalized metal oxides as the photoanode, platinum as the counter electrode, and 0.2 M/0.02 M Co(bpy)₃^{2+/3+} as the redox mediator in 0.1 M LiClO₄ MeCN (Figure 7a). The photoanode is composed of a TiO2lAl2O3 core-shell structure. The TiO₂ core was selected because its conduction band energy is sufficiently low $(E_{\text{TiO}_2}^{\text{CB}} = -0.5 \text{ V vs NHE})^{53}$ to act as an electron acceptor for excited states of 1. The Al₂O₃ oxide shell is inserted as a tunneling barrier to increase the spatial separation between the dye and semiconductor and effectively slows electron injection dynamics. 74-76 As originally proposed by Michl²¹ and then first implemented by Johnson et al.,³⁵ the tunneling barrier is necessary to slow electron injection from the singlet excited state such that SF becomes the dominant decay process from the singlet excited state. Then, because of its long lifetime, the resulting triplet excited state can be harnessed, regardless of the slowed injection rate. The TiO21 Al₂O₃ core-shell metal oxide was prepared by atomic layer deposition (ALD) using alternating cycles of AlMe₃ and H₂O on a nanocrystalline $Ti\tilde{O}_2$ film. The approximate thickness of the Al₂O₃ layer is 0.1 nm per cycle.

Two different dyes were used for the device measurements, 1 and DPPA. While the former can undergo SF, the latter does not, as indicated by the relatively high fluorescence quantum yield on ZrO_2 (Φ_{FL} = 0.90), and thus, DPPA can serve as a



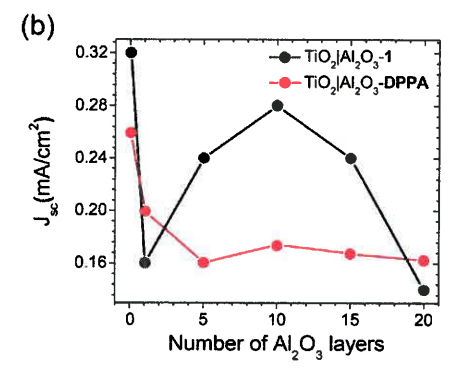


Figure 7. (a) Energy level diagram for TiO2|Al2O3-1 and dynamics events with beneficial and inhibitory processes in green and red, respectively. (b) Short circuit photocurrent density with respect to number of layers of Al₂O₃ in TiO₂|Al₂O₃-1 and TiO₂|Al₂O₃-DPPA anodes under AM1.5 illumination.

control sample that exhibits electron injection from the singlet excited state only.

Figure 7b shows the short-circuit photocurrent density for TiO2|Al2O3-1 and TiO2|Al2O3-DPPA under AM1.5 solar irradiation with respect to the thickness of the Al2O3 layers. For TiO₂lAl₂O₃-DPPA there is a decrease in photocurrent as the Al₂O₃ thickness increases. This result is consistent with previous reports of slowed injection from standard DSSC dyes. 74-76 In contrast, for the TiO2lAl2O3-1 device, there is an initial sharp decrease in J_{sc} with one layer of Al₂O₃, a gradual increase up to 10 layers of Al₂O₃, and then decrease above 10 layers. Interestingly, the photocurrent with 10 layers is only ~10% lower than that for direct electron injection (0 layers). This unusual behavior can be rationalized as follows. For 1 directly on TiO2, electron injection occurs solely from the singlet excited state of 1 $(k_{ini}(S))$. Upon addition of one layer of Al_2O_3 , electron injection is slowed resulting in a decrease in J_{sc} As the thickness of the Al_2O_3 layer increases, electron injection from the singlet state is slowed and SF (k_{SF}) followed by electron transfer from the triplet state of 1 to TiO_2 $(k_{inj(T)})$ becomes competitive. The increase in J_{sc} up to 10 layers is presumably due to exciton and charge carrier multiplication associated with SF.

Table 2 and Figures S5 and S6 show the current voltage (J-V) characteristics of the DSSC with 0 and 10 layers of Al₂O₃.

Table 2. J-V Data for TiO₂|Al₂O₃-1 and TiO₂|Al₂O₃-DPPA with 0 and 10 Layers of Al₂O₃

dye	layers of Al ₂ O ₃	$J_{\rm sc}~({\rm mA~cm^{-2}})$	$V_{\rm oc}~({\rm mV})$	η (%)
1	0	0.33	20	2.4×10^{-4}
DPPA	0	0.26	45	3.0×10^{-3}
1	10	0.28	45	3.5×10^{-3}
DPPA	10	0.17	30	1.3×10^{-3}

The poor efficiencies of the devices are likely due to a combination of (1) poor spectral overlap between the dye and the AM1.5 spectrum, (2) less than unity SF efficiency, (3) quenching of the triplet excited states by the $Co^{2+/3+}$ mediator, and (4) the standard DSSC loss pathways (e.g. recombination, slow regeneration (k_{regen}), etc.) that occur in nonoptimized devices.

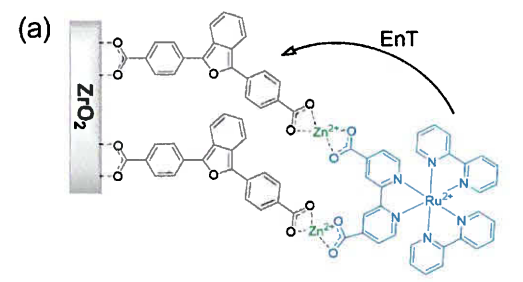
Similar to what was observed with emission, magnetic field dependent measurements of photocurrent (Figure S7) did not exhibit any of the characteristic features previously reported for SF device (i.e., an increase and then decrease in photocurrent). The field dependent response for DPPA, TiO₂-1, and TiO₂lAl₂O₃-1 were similar, suggesting that the changes in photocurrent are due to field dependence of non-SF events, like electron transport and charge extraction to the external circuit. However, as noted above and in the literature, ²⁰ while the lack of magnetic field dependence does not support a SF mechanism, it does not preclude it either, especially given that field dependence for SF in DPIBF has never been reported.

Self-Assembled Bilayer. It is important to note that, regardless of the device architecture, even if SF is harnessed at 200% efficiencies, it is not enough to exceed the SQ limit. Instead, the high energy absorption of the SF chromophore must be supplemented by a low energy light absorbing material. For the DSSC architecture described here, this could be achieved by coadsorbing the SF dye and the low energy absorbing dye on the metal oxide surface. However, due to surface area limitation, codeposition decreases the total surface loading and light absorption by each dye relative to the fully loaded monolayer film. Additionally, codeposition may inhibit the intermolecular interactions necessary for SF. ^{19,20,23,34,79}

Here we introduce self-assembled bilayers via metal ion linkages as an alternative strategy for coupling SF and low energy absorbing dyes (Figure 8a). 34,40,69,80 In contrast to codeposition, in this architecture, dye adsorption is additive, not competitive, and directional energy and electron transfer toward the surface can be achieved via energetic tuning of the low energy dye. 81 As such, the low energy dye can either directly inject electrons into the semiconductor or can participate in a sequential electron/energy transfer process involving the SF dye.

A bilayer film composed of 1 and RuC on ZrO₂ (ZrO₂-1-Zn-RuC) is depicted in Figure 8a. As a simple proof-of-concept demonstration of this architecture, Zn²⁺ was chosen as the linking ion because it is a photo- and electrochemically inert, ^{82,83} and RuC was chosen as the second dye because it readily forms a bilayer film⁶⁹ and can transfer triplet excited state energy to 1 (vide supra).

The bilayer film can be prepared by a simple stepwise soaking procedure. ⁸⁰ First, a fully loaded ZrO₂-1 film was soaked in a solution of 200 μ M Zn(OAc)₂ in MeCN and the metal ion coordination was monitored using ATR-IR (Figure S8). The shift of the C=O stretching mode from 1665 to



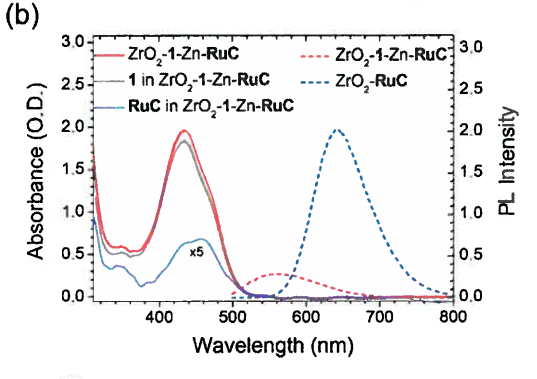


Figure 8. (a) Schematic representation of the self-assembled bilayer $(ZrO_2-1-Zn-RuC)$, and (b) absorption spectrum of the bilayer and the relative emission intensity for $ZrO_2-1-Zn-RuC$ and ZrO_2-RuC in MeCN ($\lambda_{exc} = 470$ nm).

1660 cm⁻¹ as well as the increased absorbance for the peaks between 1595 and 1415 cm⁻¹ are indicative of Zn²⁺ coordination to the nonsurface bound COOH groups of 1.⁸⁴ All spectral shifts were complete after only 15 min of soaking, indicating complete formation of ZrO₂-1-Zn.

The bilayer was then prepared by soaking the ZrO2-1-Zn film in a 200 μ M solution of RuC in acetonitrile for 5 min. The RuC soaking time was intentionally kept short to prevent competitive desorption of 1 from the surface. However, it is worth noting that an appropriate modification to the molecular structure or surface binding group affinity/stability could be used to optimize surface loadings.85 Regardless, the above results are consistent with formation of a ZrO2-1-Zn-RuC bilayer structure resembling the scheme in Figure 8a and not a codeposited film. Currently we have no direct information about local coordination chemistry or relative orientation of the dyes and so Figure 8a should be considered as a reasonable but unsupported representation. The absorption spectrum of the resulting ZrO₂-1-Zn-RuC film is shown in Figure 8b. Spectral deconvolution for each of the components was used to determine a 1 to RuC loading ratio of ~5:1.

Upon excitation at 470 nm, emission from the 3 MLCT state of RuC in ZrO₂-1-Zn-RuC ($\lambda_{max} = 650$ nm) is completely quenched relative to RuC directly on ZrO₂ (ZrO₂-RuC). Even correcting for competitive absorption by 1 at the excitation wavelength, these results indicate that there is ~100% efficient triplet energy transfer from RuC to 1 in the bilayer film. On TiO₂ in a device, 3 1* can then inject electrons into TiO₂ with RuC effectively behaving as a triplet sensitizing antenna in the SF film.

These results indicate that self-assembled bilayers could be an effective strategy to combine low energy absorbers with SF chromophores. With that said, there are a few important caveats with this strategy. The first is that unlike with RuC in the ZrO₂-1-Zn-RuC film, to be complementary to 1 the low energy dye would need to absorb light of wavelength longer than 500 nm and with no spectral overlap with 1 in the high energy region of the spectrum. Second, like RuC, the dye would also need to either act as a triplet sensitizer for 1 or have sufficient potential to inject electrons directly into TiO₂ from the singlet excited state. Finally, it is currently unclear if the formation of the bilayer hinders or helps the intermolecular interactions necessary for SF in the first layer of molecules. As depicted in Figure 8a, one could envision that the second dye, or any molecule for that matter, could be used to tune the distance and relative orientation of two SF dyes.

CONCLUSIONS

In summary, we report the photophysical properties of dicarboxylated 1,3-diphenylisobenzofuran (1) bound to nanocrystalline ZrO2 and TiO2 metal oxide films. This relatively stable dye can be synthesized in six steps and binds to the surface obeying isotherm behavior with the molecular packing density readily controlled by varying the concentration of the loading solution. The emission intensity from 1 sharply decreases with increased surface loading and is accompanied by weak excimer emission at full surface coverage. The formation of long-lived triplet states that are consistent with singlet fission were observed using nanosecond-microsecond TA spectroscopy. However, the evolution of these triplets is highly complex and could not be definitively assigned with our TA experiments. Possible contribution of excimers and/or charge-transfer states to the spectral changes has been proposed, but further temperature, excitation energy, solvent, and fluence dependence measurements are needed to fully elucidate the mechanism.

The dye was then bound to a TiO2lAl2O3 core-shell structure where the insulating Al2O3 barrier acts to slow excited state electron injection dynamics. For the TiO2|Al2O3-1 device, there is an initial sharp decrease in Jsc, a gradual increase, and then a decrease with respect to the thickness of Al₂O₃. This unusual decrease-increase-decrease behavior is in sharp contrast to a standard DSSC dye where photocurrent decreases with increasing Al₂O₃ thickness, and it is consistent with a mechanism involving singlet excitation, singlet fission, and electron injection from the triplet state. We also demonstrate that a metal-ion-linked self-assembled bilayer is an effective means of incorporating a low energy absorbing dye into the SF scheme. Near unity triplet energy transfer yields in the bilayer film as well as our proof-of-concept device are critical stepping stones toward a solar cell that can feasibly surpass the Shockley-Queisser limit by harnessing both high energy SF and low energy light.

■ ASSOCIATED CONTENT

S Supporting Information

The Supporting Information is available free of charge on the ACS Publications website at DOI: 10.1021/acs.jpcc.8b08599.

Synthesis and characterization of 1, magnetic field dependence of emission spectra and photocurrent, single wavelength kinetic traces, ns TA spectra for the sensitized film, emission quenching in solution, I-V curves, and ATR-IR absorbance for zinc loading (PDF)

AUTHOR INFORMATION

Corresponding Author

*(K.H.) E-mail: hanson@chem.fsu.edu.

ORCID 0

Sean P. Hill: 0000-0001-7625-3395

A. Eugene DePrince, III: 0000-0003-1061-2521

Mark D. Losego: 0000-0002-9810-9834 Kenneth Hanson: 0000-0001-7219-7808

Present Addresses

§Max Planck Institute for Solid State Research, Heisenbergstraße 1, 70569 Stuttgart, Germany

¹Department of Chemistry, University of Tennessee, Knoxville, TN 37996-1600

Author Contributions

The manuscript was written through contributions of all authors. All authors have given approval to the final version of the manuscript.

Notes

The authors declare no competing financial interest.

ACKNOWLEDGMENTS

The authors would like to thank the Florida State University's Energy and Materials Initiative for facilitating aspects of this research. K.H. acknowledges the support from The National Science Foundation under Grant No. DMR-1752782. V.D.K. acknowledges the support from The National Science Foundation under Grant CHE-1802240. B.D.P. acknowledges support from the National Defense Science & Engineering Graduate (NDSEG) Fellowship Program. Nanosecond transient absorption measurements were performed on a spectrometer supported by the National Science Foundation under Grant No. CHE-1531629. We would also like to thank Christopher J. Dares (Florida International University) for designing and building the magnetic field dependent measurement apparatus.

REFERENCES

- (1) Shockley, W.; Queisser, H. J. Detailed Balance Limit of Efficiency of p-n Junction Solar Cells. J. Appl. Phys. 1961, 32, 510–519.
- (2) Semonin, O. E.; Luther, J. M.; Beard, M. C. Quantum Dots for Next-Generation Photovoltaics. *Mater. Today* **2012**, *15*, 508–515.
- (3) Hanna, M. C.; Nozik, A. J. Solar Conversion Efficiency of Photovoltaic and Photoelectrolysis Cells With Carrier Multiplication Absorbers. J. Appl. Phys. 2006, 100, 074510.
- (4) Beard, M. C.; Johnson, J. C.; Luther, J. M.; Nozik, A. J. Multiple Exciton Generation in Quantum Dots Versus Singlet Fission in Molecular Chromophores for Solar Photon Conversion. *Philos. Trans. R. Soc., A* 2015, 373, 20140412.
- (5) Beard, M. C. Multiple Exciton Generation in Semiconductor Quantum Dots. J. Phys. Chem. Lett. 2011, 2, 1282-1288.
- (6) Walker, B. J.; Musser, A. J.; Beljonne, D.; Friend, R. H. Singlet Exciton Fission in Solution. *Nat. Chem.* 2013, 5, 1019-1024.
- (7) Tamai, Y.; Ohkita, H.; Benten, H.; Ito, S. Singlet Fission in Poly(9,9'-di-n-octylfluorene) Films. J. Phys. Chem. C 2013, 117, 10277-10284.
- (8) Le, A. K.; Bender, J. A.; Roberts, S. T. Slow Singlet Fission Observed in a Polycrystalline Perylenediimide Thin Film. J. Phys. Chem. Lett. 2016, 7, 4922-4928.
- (9) Burdett, J. J.; Müller, A. M.; Gosztola, D.; Bardeen, C. J. Excited State Dynamics in Solid and Monomeric Tetracene: The Roles of Superradiance and Exciton Fission. J. Chem. Phys. 2010, 133, 144506.

- (10) Wilson, M. W. B.; Rao, A.; Ehrler, B.; Friend, R. H. Singlet Exciton Fission in Polycrystalline Pentacene: From Photophysics toward Devices. Acc. Chem. Res. 2013, 46, 1330-1338.
- (11) Johnson, J. C.; Nozik, A. J.; Michl, J. High Triplet Yield from Singlet Fission in a Thin Film of 1,3-Diphenylisobenzofuran. J. Am. Chem. Soc. 2010, 132, 16302–16303.
- (12) Wang, C.; Tauber, M. J. High-Yield Singlet Fission in a Zeaxanthin Aggregate Observed by Picosecond Resonance Raman Spectroscopy. J. Am. Chem. Soc. 2010, 132, 13988-13991.
- (13) Martinez-Martinez, L. A.; Du, M.; Ribeiro, R. F.; Kéna-Cohen, S.; Yuen-Zhou, J. Polariton-Assisted Singlet Fission in Acene Aggregates. J. Phys. Chem. Lett. 2018, 9, 1951–1957.
- (14) Johnson, J. C.; Akdag, A.; Zamadar, M.; Chen, X.; Schwerin, A. F.; Paci, I.; Smith, M. B.; Havlas, Z.; Miller, J. R.; Ratner, M. A.; et al. Toward Designed Singlet Fission: Solution Photophysics of Two Indirectly Coupled Covalent Dimers of 1,3-Diphenylisobenzofuran. J. Phys. Chem. B 2013, 117, 4680–4695.
- (15) Sanders, S. N.; Kumarasamy, E.; Pun, A. B.; Trinh, M. T.; Choi, B.; Xia, J.; Taffet, E. J.; Low, J. Z.; Miller, J. R.; Roy, X.; et al. Quantitative Intramolecular Singlet Fission in Bipentacenes. *J. Am. Chem. Soc.* 2015, 137, 8965–8972.
- (16) Carey, T. J.; Snyder, J. L.; Miller, E. G.; Sammakia, T.; Damrauer, N. H. Synthesis of Geometrically Well-Defined Covalent Acene Dimers for Mechanistic Exploration of Singlet Fission. *J. Org. Chem.* 2017, 82, 4866–4874.
- (17) Korovina, N. V.; Das, S.; Nett, Z.; Feng, X.; Joy, J.; Haiges, R.; Krylov, A. I.; Bradforth, S. E.; Thompson, M. E. Singlet Fission in a Covalently Linked Cofacial Alkynyltetracene Dimer. J. Am. Chem. Soc. 2016, 138, 617–627.
- (18) Gradinaru, C. C.; Kennis, J. T. M.; Papagiannakis, E.; van Stokkum, I. H. M.; Cogdell, R. J.; Fleming, G. R.; Niederman, R. A.; van Grondelle, R. An Unusual Pathway of Excitation Energy Deactivation in Carotenoids: Singlet-to-Triplet Conversion on an Ultrafast Timescale in A Photosynthetic Antenna. *Proc. Natl. Acad. Sci. U. S. A.* 2001, 98, 2364–2369.
- (19) Smith, M. B.; Michl, J. Singlet Fisssion. Chem. Rev. 2010, 110, 6891-6936.
- (20) Smith, M. B.; Michl, J. Recent Advances in Singlet Fission. Annu. Rev. Phys. Chem. 2013, 64, 361-386.
- (21) Paci, I.; Johnson, J. C.; Chen, X.; Rana, G.; Popović, D.; David, D. E.; Nozik, A. J.; Ratner, M. A.; Michl, J. Singlet Fission for Dye-Sensitized Solar Cells: Can a Suitable Sensitizer Be Found? *J. Am. Chem. Soc.* 2006, 128, 16546—16553.
- (22) Zeng, T.; Ananth, N.; Hoffmann, R. Seeking Small Molecules for Singlet Fission: A Heteroatom Substitution Strategy. *J. Am. Chem. Soc.* **2014**, *136*, 12638–12647.
- (23) Ito, S.; Nagami, T.; Nakano, M. J. Molecular Design for Efficient Singlet Fission. J. Photochem. Photobiol., C 2018, 34, 85-120.
- (24) Zeng, T.; Goel, P. Design of Small Intramolecular Singlet Fission Chromophores: An Azaborine Candidate and General Small Size Effects. J. Phys. Chem. Lett. 2016, 7, 1351–1358.
- (25) Kawata, S.; Pu, Y.-J.; Saito, A.; Kurashige, Y.; Beppu, T.; Katagiri, H.; Hada, M.; Kido, J. Singlet Fission of Non-polycyclic Aromatic Molecules in Organic Photovoltaics. *Adv. Mater.* **2016**, 28, 1585–1500.
- (26) Ehrler, B.; Musselman, K. P.; Böhm, M. L.; Friend, R. H.; Greenham, N. C. Hybrid Pentacene/a-Silicon Solar Cells Utilizing Multiple Carrier Generation via Singlet Exciton Fission. *Appl. Phys. Lett.* 2012, 101, 153507.
- (27) Pazos-Outón, L. M.; Lee, J. M.; Futscher, M. H.; Kirch, A.; Tabachnyk, M.; Friend, R. H.; Ehrler, B. A Silicon-Singlet Fission Tandem Solar Cell Exceeding 100% External Quantum Efficiency with High Spectral Stability. ACS Energy Lett. 2017, 2, 476–480.
- (28) Ehrler, B.; Wilson, M. W. B.; Rao, A.; Friend, R. H.; Greenham, N. C. Singlet Exciton Fission-Sensitized Infrared Quantum Dot Solar Cells. *Nano Lett.* **2012**, *12*, 1053–1057.
- (29) Tabachnyk, M.; Ehrler, B.; Bayliss, S.; Friend, R. H.; Greenham, N. C. Triplet Diffusion in Singlet Exciton Fission Sensitized Pentacene Solar Cells. *Appl. Phys. Lett.* **2013**, *103*, 153302.

- (30) Thompson, N. J.; Congreve, D. N.; Goldberg, D.; Menon, V. M.; Baldo, M. A. Slow Light Enhanced Singlet Exciton Fission Solar Cells with a 126% Yield of Electrons Per Photon. *Appl. Phys. Lett.* **2013**, *103*, 263302.
- (31) Congreve, D. N.; Lee, J.; Thompson, N. J.; Hontz, E.; Yost, S. R.; Reusswig, P. D.; Bahlke, M. E.; Reineke, S.; Van Voorhis, T.; Baldo, M. A. External Quantum Efficiency Above 100% in a Singlet-Exciton-Fission—Based Organic Photovoltaic Cell. *Science* 2013, 340, 334—337.
- (32) MacQueen, R. W.; Liebhaber, M.; Niederhausen, J.; Mews, M.; Gersmann, C.; Jäckle, S.; Jäger, K.; Tayebjee, M. J. Y.; Schmidt, T. W.; Rech, B.; et al. Crystalline Silicon Solar Cells with Tetracene Interlayers: The Path to Silicon-Singlet Fission Heterojunction Devices. *Mater. Horiz.* 2018, 5, 1065.
- (33) Xia, J.; Sanders, S. N.; Cheng, W.; Low, J. Z.; Liu, J.; Campos, L. M.; Sun, T. Singlet Fission: Progress and Prospects in Solar Cells. Adv. Mater. 2017, 29, 1601652.
- (34) Wang, J. C.; Hill, S. P.; Dilbeck, T.; Ogunsolu, O. O.; Banerjee, T.; Hanson, K. Multimolecular Assemblies on High Surface Area Metal Oxides and Their Role in Interfacial Energy and Electron Transfer. Chem. Soc. Rev. 2018, 47, 104–148.
- (35) Schrauben, J. N.; Zhao, Y.; Mercado, C.; Dron, P. I.; Ryerson, J. L.; Michl, J.; Zhu, K.; Johnson, J. C. Photocurrent Enhanced by Singlet Fission in a Dye-Sensitized Solar Cell. ACS Appl. Mater. Interfaces 2015, 7, 2286–2293.
- (36) Pace, N. A.; Arias, D. H.; Granger, D. B.; Christensen, S.; Anthony, J. E.; Johnson, J. C. Dynamics of Singlet fission and Electron Injection in Self-Assembled Acene Monolayers on Titanium Dioxide. *Chem. Sci.* 2018, 9, 3004–3013.
- (37) Kunzmann, A.; Gruber, M.; Casillas, R.; Zirzlmeier, J.; Stanzel, M.; Peukert, W.; Tykwinski, R. K.; Guldi, D. M. Singlet Fission for Photovoltaics Reaching 130% Injection Efficiency. *Angew. Chem., Int. Ed.* 2018, 57, 10742—10747.
- (38) Hill, S. P.; Hanson, K. Harnessing Molecular Photon Upconversion in a Solar Cell at Sub-solar Irradiance: Role of the Redox Mediator. J. Am. Chem. Soc. 2017, 139, 10988–10991.
- (39) Gillaizeau-Gauthier, I.; Odobel, F.; Alebbi, M.; Argazzi, R.; Costa, E.; Bignozzi, C. A.; Qu, P.; Meyer, G. J. Phosphonate-Based Bipyridine Dyes for Stable Photovoltaic Devices. *Inorg. Chem.* 2001, 40, 6073–6079.
- (40) Hill, S. P.; Banerjee, T.; Dilbeck, T.; Hanson, K. Photon Upconversion and Photocurrent Generation via Self-Assembly at Organic-Inorganic Interfaces. J. Phys. Chem. Lett. 2015, 6, 4510-4517
- (41) Sapp, S. A.; Elliott, C. M.; Contado, C.; Caramori, S.; Bignozzi, C. A. Substituted Polypyridine Complexes of Cobalt(II/III) as Efficient Electron-Transfer Mediators in Dye-Sensitized Solar Cells. J. Am. Chem. Soc. 2002, 124, 11215–11222.
- (42) Shao, Y.; Gan, Z.; Epifanovsky, E.; Gilbert, A. T. B.; Wormit, M.; Kussmann, J.; Lange, A. W.; Behn, A.; Deng, J.; Feng, X.; et al. Advances in Molecular Quantum Chemistry Contained in the Q-Chem 4 Program Package. *Mol. Phys.* 2015, 113, 184–215.
- (43) Pavlishchuk, V. V.; Addison, A. W. Conversion Constants for Redox Potentials Measured Versus Different Reference Electrodes in Acetonitrile Solutions at 25°C. *Inorg. Chim. Acta* 2000, 298, 97–102.
- (44) de Mello, J. C.; Wittmann, H. F.; Friend, R. H. An Improved Experimental Determination of External Photoluminescence Quantum Efficiency. Adv. Mater. 1997, 9, 230–232.
- (45) Juris, A.; Balzani, V.; Barigelletti, F.; Campagna, S.; Belser, P.; von Zelewsky, A. Ru(II) Polypyridine Complexes: Photophysics, Photochemistry, Eletrochemistry, and Chemiluminescence. *Coord. Chem. Rev.* 1988, 84, 85–277.
- (46) Ogunsolu, O. O.; Wang, J. C.; Hanson, K. Inhibiting Interfacial Recombination Events in Dye-Sensitized Solar Cells using Self-Assembled Bilayers. ACS Appl. Mater. Interfaces 2015, 7, 27730–27734.
- (47) Arian, D.; Cló, E.; Gothelf, K. V.; Mokhir, A. A Nucleic Acid Dependent Chemical Photocatalysis in Live Human Cells. *Chem. Eur. J.* 2010, 16, 288–295.

- (48) Schwerin, A. F.; Johnson, J. C.; Smith, M. B.; Sreearunothai, P.; Popović, D.; Cerny, J.; Havlas, Z.; Paci, I.; Akdag, A.; MacLeod, M. K.; et al. Toward Designed Singlet Fission: Electronic States and Photophysics of 1,3-Diphenylisobenzofuran. *J. Phys. Chem. A* 2010, 114, 1457–1473.
- (49) Ryerson, J. L.; Schrauben, J. N.; Ferguson, A. J.; Sahoo, S. C.; Naumov, P.; Havlas, Z.; Michl, J.; Nozik, A. J.; Johnson, J. C. Two Thin Film Polymorphs of the Singlet Fission Compound 1,3-Diphenylisobenzofuran. J. Phys. Chem. C 2014, 118, 12121–12132.
- (50) Schrauben, J. N.; Ryerson, J. L.; Michl, J.; Johnson, J. C. Mechanism of Singlet Fission in Thin Films of 1,3-Diphenylisobenzofuran. J. Am. Chem. Soc. 2014, 136, 7363-7373.
- (51) Dron, P. I.; Michl, J.; Johnson, J. C. Singlet Fission and Excimer Formation in Disordered Solids of Alkyl-Substituted 1,3-Diphenylisobenzofurans. J. Phys. Chem. A 2017, 121, 8596—8603.
- (52) Johnson, J. C.; Michl, J. 1,3-Diphenylisobenzofuran: a Model Chromophore for Singlet Fission. *Top. Curr. Chem.* **2017**, 375, 80.
- (53) Katoh, R.; Furube, A.; Yoshihara, T.; Hara, K.; Fujihashi, G.; Takano, S.; Murata, S.; Arakawa, H.; Tachiya, M. Efficiencies of Electron Injection from Excited N3 Dye into Nanocrystalline Semiconductor (ZrO₂, TiO₂, ZnO, Nb₂O₅, SnO₂, In₂O₃) Films. J. Phys. Chem. B **2004**, 108, 4818–4822.
- (54) Zhou, Y.; Ayad, S.; Ruchlin, C.; Posey, V.; Hill, S. P.; Wu, Q.; Hanson, K. Examining the Role of Acceptor Molecule Structure in Self-Assembled Bilayers: Surface Loading, Stability, Energy Transfer, and Upconverted Emission. *Phys. Chem. Chem. Phys.* **2018**, 20, 20513–20524.
- (55) Zhou, Y.; Hill, S. P.; Hanson, K. Influence of meta- and paraphosphonated diphenylanthracene on photon upconversion in self-assembled bilayers. *J. Photonics Energy* **2018**, *8*, 022004.
- (56) Butler, M. A.; Ginley, D. S. Prediction of Flatband Potentials at Semiconductor-Electrolyte Interfaces from Atomic Electronegativities. *J. Electrochem. Soc.* 1978, 125, 228–232.
- (57) Dilbeck, T.; Hill, S. P.; Hanson, K. Harnessing Molecular Photon Upconversion at Sub-Solar Irradiance Using Dual Sensitized Self-Assembled Trilayers. J. Mater. Chem. A 2017, 5, 11652–11660.
- (58) Dilbeck, T.; Wang, J. C.; Zhou, Y.; Olsson, A.; Sykora, M.; Hanson, K. Elucidating the Energy- and Electron-Transfer Dynamics of Photon Upconversion in Self-Assembled Bilayers. J. Phys. Chem. C 2017, 121, 19690—19698.
- (59) Bell, T. D. M.; Pagba, C.; Myahkostupov, M.; Hofkens, J.; Piotrowiak, P. Inhomogeneity of Electron Injection Rates in Dye-Sensitized TiO₂: Comparison of the Mesoporous Film and Single Nanoparticle Behavior. J. Phys. Chem. B 2006, 110, 25314–25321.
- (60) Hosoyamada, M.; Yanai, N.; Ogawa, T.; Kimizuka, N. Molecularly Dispersed Donors in Acceptor Molecular Crystals for Photon Upconversion under Low Excitation Intensity. *Chem. Eur. J.* 2016, 22, 2060–2067.
- (61) Lissau, J. S.; Gardner, J. M.; Morandeira, A. Photon Upconversion on Dye-Sensitized Nanostructured ZrO₂ Films. *J. Phys. Chem. C* **2011**, *115*, 23226–23232.
- (62) Lissau, J. S.; Nauroozi, D.; Santoni, M. P.; Ott, S.; Gardner, J. M.; Morandeira, A. Anchoring Energy Acceptors to Nanostructured ZrO₂ Enhances Photon Upconversion by Sensitized Triplet-Triplet Annihilation Under Simulated Solar Flux. *J. Phys. Chem. C* **2013**, *117*, 14493–14501.
- (63) Zhang, Y.; Lei, Y.; Zhang, Q.; Xiong, Z. Thermally Activated Singlet Exciton fission Observed in Rubrene Doped Organic films. Org. Electron. 2014, 15, 577-581.
- (64) Dillon, R. J.; Piland, G. B.; Bardeen, C. J. Different Rates of Singlet Fission in Monoclinic versus Orthorhombic Crystal Forms of Diphenylhexatriene. J. Am. Chem. Soc. 2013, 135, 17278–17281.
- (65) Zimmerman, P. M.; Zhang, Z.; Musgrave, C. B. Singlet Fission in Pentacene Through Multi-Exciton Quantum States. *Nat. Chem.* **2010**, *2*, 648–652.
- (66) Lee, J.; Jadhav, P.; Baldo, M. A. High Efficiency Organic Multilayer Photodetectors Based on Singlet Exciton Fission. *Appl. Phys. Lett.* **2009**, 95, 033301.

- (67) Thompson, N. J.; Hontz, E.; Chang, W.; Van Voorhis, T.; Baldo, M. Magnetic Field Dependence of Singlet Fission in Solutions of Diphenyl Tetracene. *Philos. Trans. R. Soc., A* 2015, 373, 20140323.
- (68) Banerjee, T.; Biswas, A. K.; Reddy G, U.; Sahu, T. S.; Das, A.; Ganguly, B.; Ghosh, H. N. Superior Grafting and State-of-the-Art Interfacial Electron Transfer Rates for Newly Designed Geminal Dicarboxylate Bound Ruthenium(II)—and Osmium(II)—Polypyridyl Dyes on TiO₂ Nanosurface. J. Phys. Chem. C 2014, 118, 3864—3877.
- (69) Wang, J. C.; Murphy, I. A.; Hanson, K. Modulating Electron Transfer Dynamics at Dye–Semiconductor Interfaces via Self-Assembled Bilayers. J. Phys. Chem. C 2015, 119, 3502–3508.
- (70) Michl, J. Singlet-Fission Sensitizers for Ultra-High Efficiency Excitonic Solar Cells; Subcontract Report NREL/SR-520-44685; National Renewable Research Laboratory: Golden, CO, 2008.
- (71) Dover, C. B.; Gallaher, J. K.; Frazer, L.; Tapping, P. C.; Petty, A. J., II; Crossley, M.; Anthony, J. E.; Kee, T. W.; Schmidt, T. W. Endothermic Singlet Fission is Hindered by Excimer Formation. *Nat. Chem.* 2018, 10, 305–310.
- (72) Monahan, N.; Zhu, X.-Y. Charge-Transfer Mediated Singlet Fission. Annu. Rev. Phys. Chem. 2015, 66, 601-618.
- (73) Lukman, S.; Chen, K.; Hodgkiss, J. M.; Turban, D. H. P.; Hine, N. D. M.; Dong, S.; Wu, J.; Greenham, N. C.; Musser, A. J. Tuning the Role of Charge-Transfer States in Intramolecular Singlet Exciton Fission Through Side-Group Engineering. *Nat. Commun.* 2016, 7, 13622.
- (74) Prasittichai, C.; Avila, J. R.; Farha, O. K.; Hupp, J. T. Systematic Modulation of Quantum (Electron) Tunneling Behavior by Atomic Layer Deposition on Nanoparticulate SnO₂ and TiO₂ Photoanodes. *J. Am. Chem. Soc.* **2013**, *135*, 16328–16331.
- (75) Palomares, E.; Clifford, J. N.; Haque, S. A.; Lutz, T.; Durrant, J. R. Control of Charge Recombination Dynamics in Dye Sensitized Solar Cells by the Use of Conformally Deposited Metal Oxide Blocking Layers. J. Am. Chem. Soc. 2003, 125, 475–482.
- (76) Antila, L. J.; Heikkila, M. J.; Mäkinen, V.; Humalamäki, N.; Laitinen, M.; Linko, V.; Jalkanen, P.; Toppari, J.; Aumanen, V.; Kemell, M.; et al. ALD Grown Aluminum Oxide Submonolayers in Dye-Sensitized Solar Cells: The Effect on Interfacial Electron Transfer and Performance. J. Phys. Chem. C 2011, 115, 16720–16729.
- (77) Kim, D. H.; Losego, M. D.; Peng, Q.; Parsons, G. N. Atomic Layer Deposition for Sensitized Solar Cells: Recent Progress and Prospects. Adv. Mater. Interfaces 2016, 3, 1600354.
- (78) Wu, T. C.; Thompson, N. J.; Congreve, D. N.; Hontz, E.; Yost, S. R.; Van Voorhis, T.; Baldo, M. A. Singlet Fission Efficiency in Tetracene-Based Organic Solar Cells. *Appl. Phys. Lett.* **2014**, *104*, 193901.
- (79) Morandeira, A.; Lopez-Duarte, I.; O'Regan, B.; Martinez-Diaz, M. V.; Forneli, A.; Palomares, E.; Torres, T.; Durrant, J. R. Ru(II)-Phthalocyanine Sensitized Solar Cells: the Influence of Co-Adsorbents Upon Interfacial Electron Transfer Kinetics. *J. Mater. Chem.* 2009, 19, 5016–5026.
- (80) Hanson, K.; Torelli, D. A.; Vannucci, A. K.; Brennaman, M. K.; Luo, H.; Alibabaei, L.; Song, W.; Ashford, D. L.; Norris, M. R.; Glasson, C. R. K.; et al. Self-Assembled Bilayer Films of Ruthenium-(II)/Polypyridyl Complexes through Layer-by-Layer Deposition on Nanostructured Metal Oxides. *Angew. Chem., Int. Ed.* 2012, 51, 12782–12785.
- (81) Ogunsolu, O. O.; Murphy, I. A.; Wang, J. C.; Das, A.; Hanson, K. Energy and Electron Transfer Cascade in Self-Assembled Bilayer Dye-Sensitized Solar Cells. ACS Appl. Mater. Interfaces 2016, 8, 28633–28640.
- (82) Wang, J. C.; Ogunsolu, O. O.; Sykora, M.; Hanson, K. Elucidating the Role of the Metal Linking Ion on the Excited State Dynamics of Self-Assembled Bilayers. J. Phys. Chem. C 2018, 122, 9835–9842.
- (83) Wang, J. C.; Violette, K.; Ogunsolu, O. O.; Cekli, S.; Lambers, E.; Fares, H. M.; Hanson, K. Self-Assembled Bilayers on Nanocrystalline Metal Oxides: Exploring the Non-Innocent Nature of the Linking Ions. *Langmuir* 2017, 33, 9609–9619.

>			

- (84) Ogunsolu, O. O.; Wang, J. C.; Hanson, K. Increasing the Open-Circuit Voltage of Dye-Sensitized Solar Cells via Metal-Ion Coordination. *Incre. Chem.* **2017**, *56*, 11168–11175.
- Coordination. Inorg. Chem. 2017, 56, 11168–11175.

 (85) Hanson, K.; Brennaman, M. K.; Luo, H.; Glasson, C. R. K.; Concepcion, J. J.; Song, W.; Meyer, T. J. Photostability of Phosphonate-Derivatized, Ru^{II} Polypyridyl Complexes on Metal Oxide Surfaces. ACS Appl. Mater. Interfaces 2012, 4, 1462–1469.